Soft Matter

Flow fluctuations in wormlike micelle fluids

Journal:	*Soft Matter*
Manuscript ID	SM-ART-08-2018-001649.R1
Article Type:	Paper
Date Submitted by the Author:	01-Oct-2018
Complete List of Authors:	Salipante, Paul; NIST Material Measurement Laboratory, Polymers and Complex Fluids Group Meek, Stephen; NIST Material Measurement Laboratory, Polymers and Complex Fluids Group Hudson, Steven; NIST Material Measurement Laboratory, Polymers and Complex Fluids Group

Soft Matter

ARTICLE TYPE

Cite this: DOI: 10.1039/xxxxxxxxxx

Flow fluctuations in wormlike micelle fluids†

Paul F. Salipante,*[a] Steven Meek,[b] and Steven D. Hudson[a]

Received Date
Accepted Date

DOI: 10.1039/xxxxxxxxxx

www.rsc.org/journalname

We investigate the unstable flow of wormlike micelle solutions in pressure driven capillary flow, with a focus on the effect of entrance geometry on the fluid fluctuations. The flow is measured at different points in the capillary using particle image velocimetry while simultaneously measuring the pressure drop across the entire capillary. The fluctuations are characterized by rapid flow rate jumps that correspond with a decrease in the pressure drop followed by a longer recovery period. Velocimetry measurements in the entrance region show a transition to unstable flow above a critical flow rate, where large flow circulations are observed in the tapered geometry and localized jets are observed in an abrupt contraction. The transition to this unstable flow is shown to occur at a similar dimensionless extension rate normalized by the micelle relaxation time. A rapid breakdown in micelle alignment is observed in polarized light microscopy at the onset of the flow rate jump, indicating the importance of rapid micelle structural changes on the fluctuations. We characterize the system by analyzing the power spectral densities and develop a dynamical systems model to describe the relationship between pressure and flow rate. These developments provide understanding to control flow fluctuations and motivation for more detailed study of the coupling of fluid microstructure transitions and flow fluctuations.

1 Introduction

The pressure driven flow of non-Newtonian fluids through pipes is common in industrial processing and high shear rate rheological measurements[1–3]. These fluids often have viscoelastic properties, making them particularly susceptible to instabilities due to the nonlinear coupling with elastic stresses, even when inertia is negligible[4–9]. The need for understanding instabilities in pipe flow has focused on applications where flow fluctuations are undesirable, such as polymer extrusion[10,11] or in material measurements including capillary rheology[12–14] and time-averaged scattering experiments[15,16]. Although such instabilities are usually avoided, certain applications may benefit from flow instabilities, such as those that require mixing at small length scales in microfluidic devices[17,18].

High shear rate viscosity measurements are frequently performed on capillary rheometers, where pressure and flow rate are measured across a narrow test capillary to determine viscosity as a function of shear rate[19]. Recently, the need for high shear rate measurements of small fluid volumes has motivated the development of microfluidic rheometers and small capillary geometries[20–22]. These devices typically have reductions and expansion in the capillary diameter, introducing extension and curvature to the streamlines where elastic instabilities are predicted to develop[5,23,24]. The onset and characteristics of these instabilities in small devices motivates this study.

Wormlike micelles (WLM) are a system of particular interest for capillary flow because of their susceptibility to instabilities arising from structural changes above a critical stress threshold which initiates strong shear-thinning behavior[25–28]. The semi-dilute concentrations are of particular interest because of their shear banding behavior, which can produce a 2 to 3 order of magnitude increase in shear rate near a critical shear stress[15,29–31]. Pressure driven flow measurements have been used to measure shear rate dependent viscosity in capillary rheometers and their flow profiles in capillary tubes[32,33]. More recently, some aspects of the micelle structure at high shear rates obtainable in pressure driven flow have been measured using small angle neutron scattering[3,34,35].

A number of pressure driven flow experiments using WLM solutions have reported persistent flow rate fluctuations which have hampered rheological and structural measurements under certain conditions[13,30,32,33,36]. The source of instabilities in pressure driven flows has however not received as much attention as those in rotational flows[37–39]. The characteristics of unstable rotational flow have been studied using both stress and shear rate controlled rheometry in combination with flow field visualizations[7,40,41]. Theoretical explanations of the spatio-temporal behavior comprise coupled evolution equations for flow and mi-

[a]National Institute of Standards and Technology, 100 Bureau Drive, Gaithersburg, MD, USA. Fax: XX XXXX XXXX; Tel: 1-301-975-2820; E-mail: paul.salipante@nist.gov
[b] Address, Address, Town, Country.

† Electronic Supplementary Information (ESI) available: [details of any supplementary information available should be included here]. See DOI: 10.1039/cXsm00000x/

crostructure[42]. These instabilities in wormlike micelle (WLM) solutions have also been studied in the context of elastic turbulence[43,44]. Turbulent behavior has also been observed in curvilinear flows of polymer solutions in microfluidic channels[45,46].

Experimental studies on pressure driven flow of WLM solutions in various microfluidic geometries have revealed other spatial instabilities in straight channels with rectangular cross-sections[47,48], as well as in curved channels and microfluidic contractions[49,50]. These spatial instabilities are typically observed in semi-dilute WLM solutions, which may exhibit shear banding[31]. The rectangular cross sections have been shown to be important for producing a spatial instability because of the varying wall stress, which leads to a jetting flow instability in an intermediate flow regime[48]. At higher flow rates, spatial undulations at the interface between shear bands have been predicted and observed for WLM solutions in rectangular cross sections[51–53].

The temporal fluctuations that have been observed in previous capillary measurements demonstrate that instabilies in axisymmetric flow geometries differ compared with those in rectangular cross sections. This difference in behavior may arise because axisymmetric geometries lack a preferred position for instabilities, and thus the flow structure fluctuates in time. For example, Hashimoto et al. (2006) investigated flow instabilities of wormlike micelles into an abrupt contraction for different surfactant and salt concentrations[54]. They observed fluctuations of the vortex region and development of turbid regions. Other investigations of the flow of WLM solutions through abrupt axisymmetric contractions include small angle neutron scattering and numerical simulations[55,56]. The rapid changes in flow behavior of wormlike micelles in axisymmetric contractions is similar to rate dependent behavior of WLM solutions observed in extensional flow[57,58], motivating this study of entrance flow.

Recent investigations of mixed flow conditions have shown the importance of the extensional flow components to unstable flow behavior. In particular, the flow around a cylinder and the motion a sedimenting sphere have been shown to produce rapid changes in flow rate, attributed to the breakdown of micelles resulting from extenstional flow[59–61]. The breakdown in micelle structure has been visualized with studies birefringence measurements and compared to the flow field[62].

In this paper, we observe the instability of wormlike micelle solutions in various capillary constriction geometries including tapers and abrupt contraction. We use synchronized pressure measurements and particle image velocimetry (PIV) to measure the transition to unstable flow and to characterize the pressure and flow rate fluctuations. Flow field instabilities in the entrance region are observed using PIV and compared to simultaneous measurements of the pressure drop. Considering relaxation times determined from rotational rheology measurements for different surfactant systems and the geometry of the constriction, the transition to unstable flow is characterized by the extension rate Weissenberg number in the entrance region. Next, we characterize the fluctuations by measuring the magnitude of flow rate jumps, time between jump events, and pressures at which an instability event is triggered. The power spectral density (PSD) of the flow rate and pressure drop data are compared to the PSD of two-sided exponential pulses. The unstable flow of WLM solutions in the entrance is compared to the flow behavior of polymer solutions. Finally, we introduce a simple model to describe the relationship between flow rate and pressure drop and compare it to experimental observations.

2 Experimental

We select three surfactant systems that form wormlike micelle structures and have been previously observed to produce spatiotemporal instabilities[25,37,39,63]. The first system is an equimolar concentration of 50 mmol/L cetyltrimethylammonium bromide (CTAB) and cosurfactant sodium salicylate (NaSal) in water. The second system is 50 mmol/L cetyltrimethylammonium tosylate (CTAT) in 100 mmol/L sodium chloride (NaCl). The third system is a 100 mmol/L cetylpyridinium chloride and 60 mmol/L NaSal in water. Two polymer based fluids are measured for comparison with the WLM solutions. The first polymer is 300 $\mu g/g$ polyacrylic acid (PAA) in glycerol with 50 mass% water. The second system is 0.2 mass% Carbopol with enough NaOH (150 uL) to achieve pH 6.

The fluid properties are measured in a Couette geometry on a strain controlled rheometer (ARES-G2, TA Instruments) *. The steady shear rheology measurements are shown in Figure 1. The relaxation time, λ, are determined from the onset of shear thinning for the three surfactant systems. They are measured to be 14 s for CTAB, 4 s for CPCL, and 2.5 s for CTAT. These three solutions each have a similar plateau stress or critical stress for shear banding.

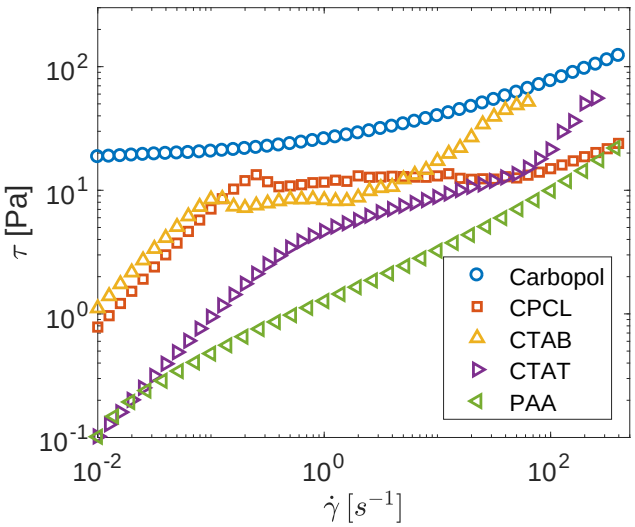

Fig. 1 Steady shear rheology of fluids in this study measured in Couette flow.

Capillary test sections with tapered entrance are made by

* Certain commercial materials and equipment are identified in this paper in order to adequately specify the experimental procedure. In no case does such identification imply recommendation or endorsement by the National Institute of Standards and Technology, nor does it imply that these are necessarily the best available for the purpose.

Capillary	narrow section radius r (mm)	narrow section length L (mm)	taper section length l (mm)
C_1	0.065	10	8
C_2	0.150	1.0	8
C_3	0.075	20	-

Table 1 Dimensions of capillary test sections represented in Figure 2.

pulling a 1.1 mm inner diameter capillary tube with a gravity driven pipette puller (Nirashige PP-83) and prevented from breaking. The range of the puller and applied heat are adjusted to make sections with different geometry. One capillary, denoted C_1, is pulled to have a narrow section of approximately 0.13 mm diameter, 10 mm in length, and tapered regions of approximately 8 mm in length on both sides. Another capillary, denoted C_2, is pulled to have a narrow section of approximately 0.30 mm diameter, 1.0 mm in length, and tapered regions of approximately 8 mm. A third test section with an abrupt contraction/expansion, denoted C_3, is made by attaching a 1.1 mm inner diameter capillary with epoxy to a 0.150 mm diameter thick-walled capillary (3 mm outer diameter). The test sections are placed between two glass slides and fixed in place using optical adhesive (Norland NOA 68), which nearly eliminates optical distortion, which would otherwise occur.

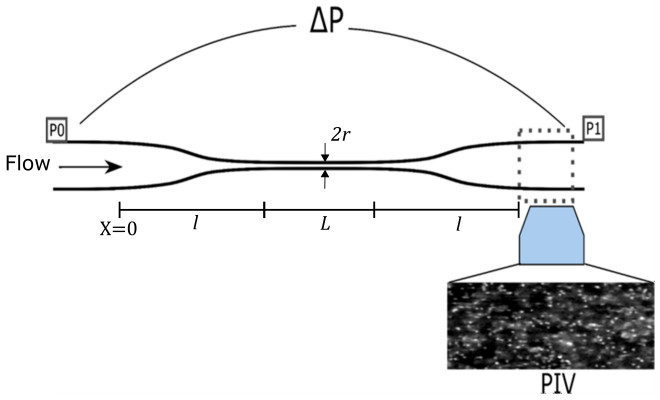

Fig. 2 Instrument setup for flow through a (tapered) capillary. The pressure difference between two pressure sensors is used to determine the pressure drop across the capillary. Images are recorded from fluorescent particles seeded in the fluid and the flow field is determined from particle image velocimetry.

The extension rate in the entrance region, $\dot{\varepsilon}$, is used to determine Weissenberg number, $Wi = \dot{\varepsilon}\lambda$. To approximate the local extension rate, we measure the radius of the capillary as a function of axial position in the entrance region and assume incompressible flow. We then estimate the maximum velocity along the centerline by integrating the shear rates from the measured shear rheology (Figure 1) to construct a velocity profile which matches the volumetric flow. The change in velocity along the center line is computed as $\dot{\varepsilon} = \frac{dV}{dx}$ for each fluid at a given flow rate. For the abrupt contraction, since the reduction in radius is large for $R_1 \approx 8R_2$, where R_1 and R_2 are the upstream and downstream capillary radii, we estimate the extension rate using the Sampson result for the Newtonian flow into a hole in a half plane[64], $\dot{\varepsilon} = \frac{Qx}{\pi(R_2^2+x^2)^2}$.

The flow for most of our experiments is controlled using a pneumatic pressure control system (Fluigent). We also drive flow with a syringe pump (Harvard Apparatus) to assess the effect of flow control on instability behavior. The fluid is delivered to the device using 1.6 mm inner diameter Tygon tubing with 1.6 mm wall thickness. The capillary ends are connected with tubing to a luer T-junction with pressure sensors inserted into one port (XP5-2BS Instrument Specialties) and the remaining port connected to the fluid reservoir. The pressure sensor readings are recorded through a data acquisition module (National Instruments). The fluids are seeded with 3 μ m fluorescent microparticles at less than 1 mL/L. Fluorescent images of the particles in flow are gathered on an inverted microscope (Olympus IX71) with a 4x objective and a ccd camera (IDT vision NR4-S2). We gather images in the straight 1.1 mm diameter portion of the capillary either upstream or downstream of the tapered section. PIV is used to measure the flow field in these sections and then flow rate is determined by integrating the velocity field in the radial direction[65]. Images are also taken in the entrance region to examine the flow field there and to compare pressure data.

The fluid is loaded through the entire flow system and checked for any trapped air. After loading, the flow control is turned off and the system is allowed to relax for at least 1 minute. Experiments are performed by incrementally increasing the applied pressure starting from the lowest test value. Observations are made at each driving flow condition after long term transient behavior is no longer observed in the pressure data, typically after about 1 min. Recordings are initiated using software that simultaneously triggers the camera to acquire an image sequence and initiate recording pressure data.

3 Results and Discussion

As the applied flow is increased in our test system, we observe a transition from steady to temporally unstable pressure drop and flow rate for all capillary sections and surfactant solutions tested. The mean flow rate where this transition occurs and the characteristics of the fluctuations depend on system parameters. At any given flow condition above this critical value, the unstable behavior persists throughout the duration of our observation.

3.1 Flow Field in Taper

Visualization of the velocity field in the mixed-flow tapered region provides insight into the instability. We focus the microscope on the center plane of the tapered region of the capillary and perform PIV analysis on the particles that are in focus. We do not determine the volumetric instantaneous flow rate from the measured velocity field in the taper because the field is highly asymmetric. Synchronization between the camera and pressure sensors shows the relationship between the flow field and the pressure drop before, during, and after an instability event.

Representative velocity fields of CPCL surfactant flowing through the C_1 capillary during one instability cycle are shown in Figure 3. The first time point shown, Fig 3(a), demonstrates the

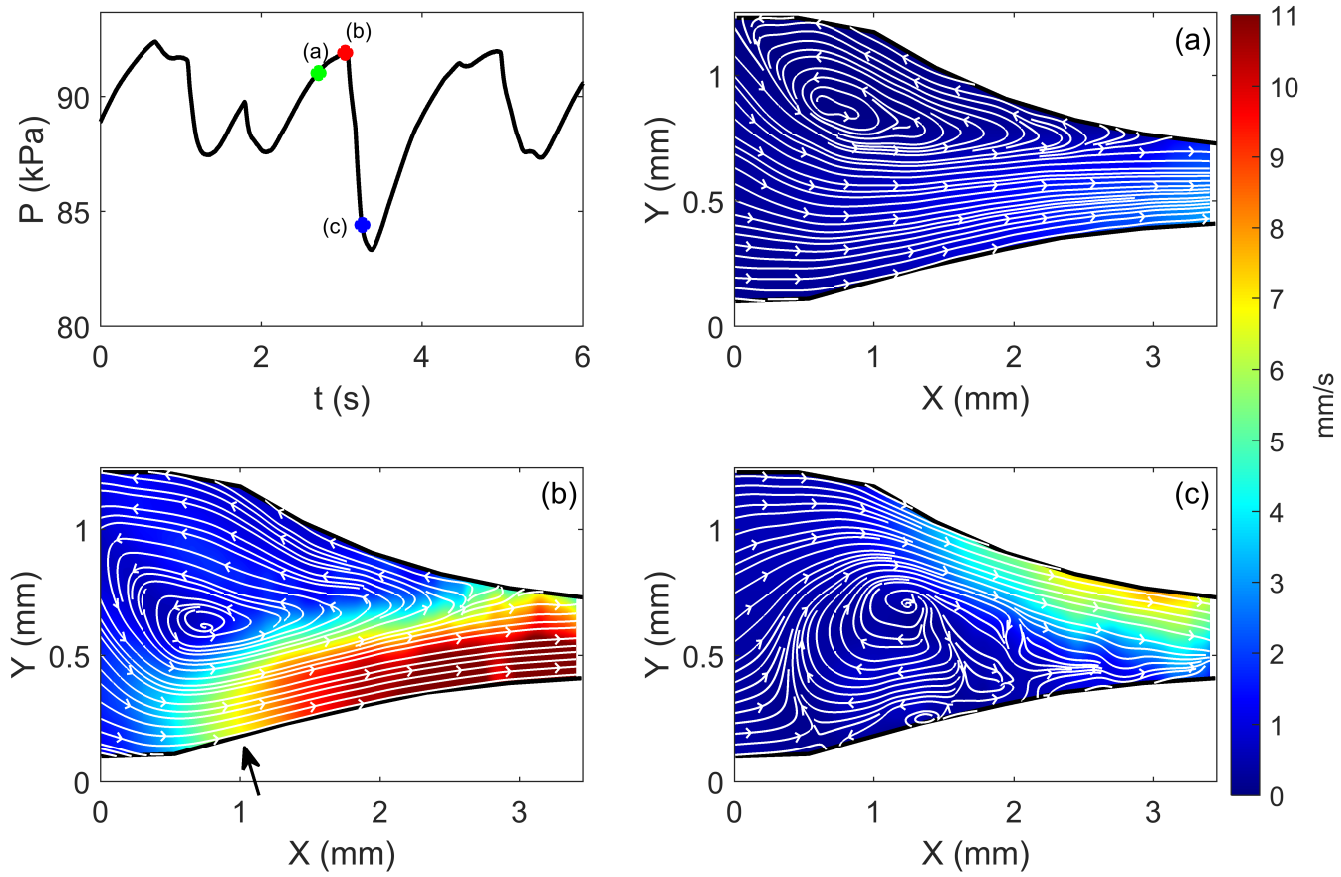

Fig. 3 Velocity field (of the CPCL solution) in the tapered region of the capillary (C_1) at three different time points indicated on the plot of pressure. The maximum Weissenberg number calculated from the mean flow rate is $Wi = \dot{\varepsilon}\lambda \approx 10$. (a) The flow is asymmetric with the dominant flow directly along the bottom side of the taper and a recirculation region on the top. (b) At peak pressure an instability event is triggered and a high velocity region forms along the bottom side of the capillary wall indicated by the arrow. The event triggers an increase in velocity throughout the tapered region as fluid is pulled in by the high velocity jet. (c) After the pressure has decreased, the high velocity region has decreased in magnitude and also changes location to the top wall.

lowest magnitude velocity field through the cycle. The primary flow in the taper is asymmetric, located along the bottom portion with a recirculation region along the top side. This flow condition persists as the pressure builds without significant change until an instability event is triggered, see Figure 3(b). The dominant direction of the flow through the taper remains along the bottom wall of the taper, but the velocity magnitude there increases dramatically. The high velocity region narrows, pulling fluid from the upstream portion of the channel and expanding the recirculation zone. Immediately after the spurt event, the pressure decreases for approximately 0.3 s. The subsequent flow field following this pressure decrease phase is shown in Fig 3(c), when the location of high flow switches to the top side. The velocity magnitude also decreases relative to the previous frame, but is still larger than the lowest velocity condition. The flow magnitude continues to decrease as the pressure increases again and the velocity field returns to a condition similar to that shown in Figure 3(a) except the primary flow direction along the top side is maintained. Only after an instability event does a shift to a new location occur, which can be from any orientation angle. The lack of a preferred direction is a consequence of the axisymmetric geometry, which does not have regions of high stress that can trigger the instability to form in a specific location.

Here we do not measure the full 3D flow field, and so we cannot model the instantaneous stress state. However, this repeated instability likely arises from internal stress imbalances and extensional flow, as described earlier.

3.2 Simultaneous Flow Rate and Pressure Drop Measurements

The instability in the tapered region influences the flow through the entire system. The rigid glass geometry and incompressibility of the fluid allow for the flow rate to be measured in the straight 1.1 mm diameter section of the capillary. We are therefore able to compare fluctuations of two lumped variables, pressure drop and flow rate, that describe the instability in the tapered region.

Examples of these simultaneous measures at various mean flow rates, given in terms of Wi number, are shown for the CTAB sys-

tem in the C_1 capillary in Figure 4. The *Wi* numbers reported here refer to the condition in 1.1 mm diameter portion of the capillary. The corresponding *Wi* in the narrow section of the capillary is much higher. The lowest *Wi* number (e.g. $Wi=2$) exhibits steady flow rate and pressure drop. At higher *Wi* number (e.g., $Wi=9$, Figure 4a(ii)), the flow in the taper is unstable and both flow rate and pressure drop fluctuate. At this *Wi* number, the fluctuations are quasi-periodic with a period of approximately 4 s. The relationship between pressure and flow rate fluctuations is most evident in this condition and is clearly shown in a pressure-flow phase plot of the same data (Figure 4(b)). In particular, a large jump in flow rate, which has been referred to as a "spurt", coincides with the peak of the pressure. This jump in flow rate matches the increased velocity observed in the taper at the maximum pressure, Fig 3(b). The flow rate rapidly reaches a maximum once the "spurt" is triggered, approximately 0.1 s after the initial increase. The pressure does not significantly decrease as the flow rate is increasing, noticeable by the flat top of the phase plot. After reaching the maximum flow rate, the pressure and flow rate both begin to decrease. The pressure reaches a minimum approximately 1 s after the maximum, while the flow rate continues to decrease gradually until the next spurt is triggered. The growth in pressure is nonlinear, following an exponential decay towards a plateau value. After approximately (4 to 5) s, the spurt is triggered again at the pressure maximum, beginning the cycle again. The pressure at which the unstable event is triggered remains fairly constant over time, indicating that a critical value is only exceeded at the maximum of the pressure cycle.

The volume of fluid released during each "spurt" event can be estimated by integrating the flow rate during each period. The volume for the data shown in Figure 4c is approximately 0.2 μL. This is comparable with an estimate for the volume of the fluidized fast-moving region in the taper of 0.25 μL (figure 3b), having approximate dimensions of (0.3 x 0.3 x 2.5) mm^3. The comparable volumes suggest that each spurt cycle is related to a portion of the entrance region that becomes fluidized. This suggests that the characteristics of the entrance region are important for understanding the unstable behavior.

A feature observed for all surfactant systems in the C_1 capillary at flow rates just above the transition to unsteady flow is a slight increase in the flow rate before a spurt is triggered. In this case the flow rate minimum does not always correspond to the beginning of the spurt cycle. An example of the flow rate data is shown in Figure 4(c). This is the only condition where both flow rate and pressure drop are increasing simultaneously, which is observable in Figure 4(a) ii-iii. We investigate the causes for this in our dynamical systems model in Section 4.

As mean flow rate is increased, the fluctuations switch from a quasi-peroidic to chaotic behavior. The average time between spurt events decreases and a broader distribution of wait times between spurts is observed. The pressure maxima are more varied and appear as sharp changes rather than slowly approaching a plateau as seen in the quasi-periodic behavior. The magnitude of flow rate jumps also varies, although the general characteristics of spurt events followed by decrease in pressure and flow rate persists. The coupling between pressure and flow rate is evident

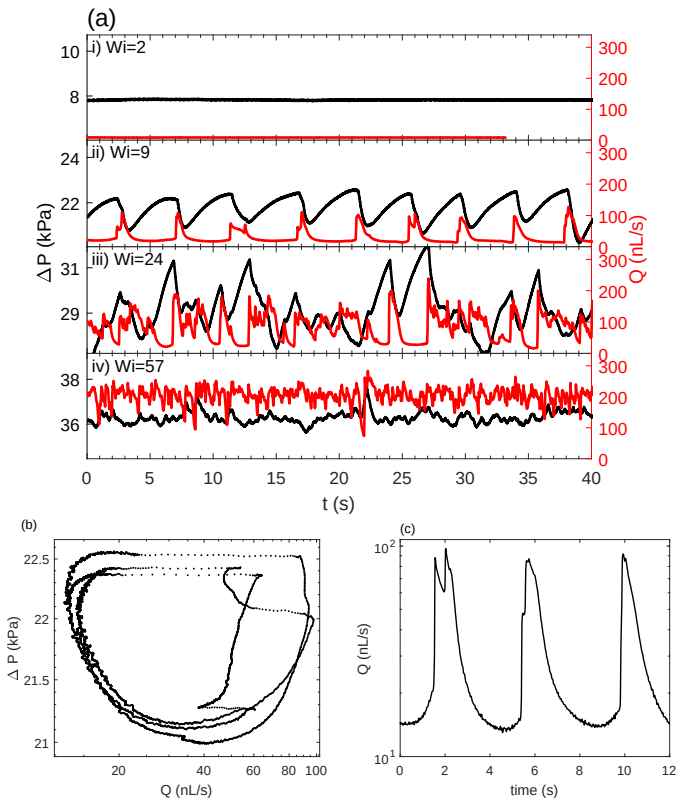

Fig. 4 (a) Time series of pressure and flow rate measurements at increasing values of *Wi* number. With increasing *Wi* number, the flow transitions from steady to quasiperiodic to chaotic. (b) Phase plot for the quasiperoidic behavior at $Wi = 9$. (c) Detail of flow rate data for $Wi = 9$ showing sequence of spurts events with short increase in flow rate before spurt.

in that the magnitude of the flow rate jump is related to the magnitude of the pressure peak. Larger magnitude flow rate jumps occur at higher pressure maxima and large spurt events are often followed by smaller flow rate fluctuations as the pressure decreases. This relationship will be investigated in more detail in the following section.

As *Wi* number increases, the long duration pressure growth periods and corresponding large magnitude flow rate jumps become less frequent. These periods are completely absent at the highest *Wi* number shown in Figure 4(a), which is characterized by only small and rapid pressure fluctuations. The flow rate fluctuations at this *Wi* are also rapid, but remarkably, the absolute magnitude of the fluctuations remain at a similar magnitude as the lower *Wi* number behavior.

3.3 Analysis of Instability Threshold

The flow field in the taper, described above in Figure 3, is reminiscent of elastic flow instabilities observed in polymeric solutions and melts. Elastic instabilities result from the stretching of polymer molecules along curved streamlines[66,67]. Coupling between the normal stress and velocity gradients along curved streamlines leads to the amplification of secondary flows. The flow through the entrance is a mixed flow, with a large extensional component at the centerline and a maximum shear rate at the wall. In the

context of mixed flow, it is difficult to apply the Pakdel-McKinley criterion to predict the onset of instability, since it assumes a flow dominated by shear[68,69]. The application of the criterion is further complicated for strongly shear thinning fluids, which changes the local velocity gradients, velocity magnitude, and polymer relaxation time, all of which affect the onset of elastic instabilities. Despite the difficulty in predicting the onset of elastic instabilities, in this section we present evidence that the onset of unstable flow arises from the extensional flow at the centerline, similar to other work of flow past a sphere or cylinder[60–62]

Measurements of WLM solution extensional rheology using opposing jets are difficult because of the onset of instabilities at high Weissenberg numbers[70]. Upon increasing extensional rate, the extensional viscosity first at increases substantially (Trouton ratios sometimes reach tens of thousand[58]). A drop in extensional viscosity at higher rates has been shown to correspond to an onset of micelle breakage[71]. This decrease in viscosity under elongational flow has also been measured using filament stretching[58], and is predicted in the context of the Vasquez–Cook–McKinley model[72]. Adjusting a parameter in that model that relates to scission energy changes the degree of extensional thickening, but breakage and associated thinning occur at similar extension rates[73].

The value of Wi along the tapered portion of the capillary is plotted in Figure 5a at the onset of unstable flow for CTAB in channel C_1. There is variation along the capillary due to the change in curvature and the increasing velocity along the entrance. The largest value for Wi occurs approximately 3 mm into the entrance.

We estimate the critical Wi value for each for various surfactant solutions and channel combinations. The critical Wi value is shown as a function of mean flow rate at the transition for the each system. The error bars show the range of values between the stable and unstable observations. Even though each system transitions to unstable flow at different flow rates, the critical Wi is in the range of 6 to 12 for each system. The abrupt entrance, C_3, has the shortest entrance region and therefore the relatively fastest extensional flow. Although we might suppose that the breakage rate itself might be an appropriate rate for extensional thinning, previous work that measures micelle breakage in extension shows that it occurs at rates modestly above the extension rate required to align the micelles[71].

The experiment with CPCL in the C_1 channel is repeated with flow driven by a syringe pump. We observe negligible difference in the flow rate and Wi number where the system goes unstable. The critical Wi number is therefore not sensitive to how the flow through the system is controlled. We will show in the next section that such control does affect the magnitude of the fluctuations.

To explore further the relationship of extensional flow, alignment and micelle breakage to trigger the unstable flow we observe the flow in the taper using a polarized light camera (CRYSTA PI-1P, Photron USA, Inc.). In this experiment, the sample is illuminated with circularly polarized light and the polarization sensitive image is then analyzed to compute the optical retardation. An image sequence of retardation magnitude is shown in Figure 6. We note that the measured signal includes birefringence from

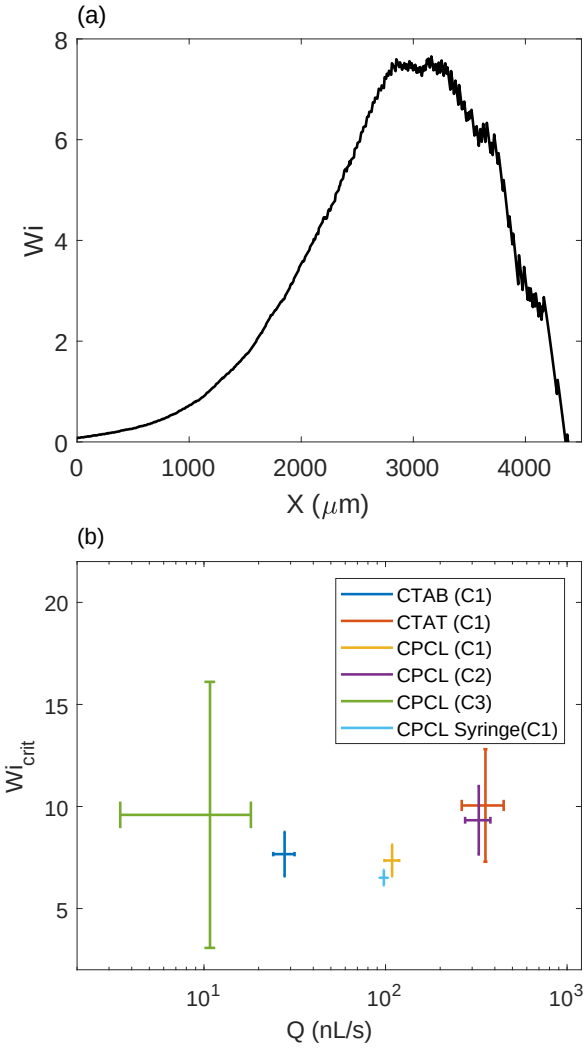

Fig. 5 (a) Local extensional Wi number along the channel for CTAB surfactant in channel C_1, where the X coordinate is the streamwise direction starting at the entrance to the tapered region. (b) Maximum value of Wi in the entrance region at the onset of unstable flow. The uncertainty range indicates the measurement values of flow rate and Wi below and above the transition to unstable flow.

the stress-optic rule and the variation of the transmission path length due to the taper in the capillary. Quantification of the birefringence to get stress is therefore challenging, but a comparison of the retardation at the same point in the video will indicate local stress changes. A strongly birefringent signal is initially observed throughout the taper and it surprisingly develops a cleavage at 0.16 s across the entire cross section, indicated by an arrow in Figure 6b). The subsequent frames illustrate a redistribution of the birefringent signal as the flow redistributes the micelles through the taper, before the process repeats.

The sharp change in birefringent signal across the entire channel cross-section shows that a breakdown in micelle structure occurs through the center line of the channel. Loss of birefringence is not anticipated by merely breaking, if the micelles maintain alignment. A rapid relaxation is thus observed here to occur in at least a portion of the fluidized volume. The breakdown of

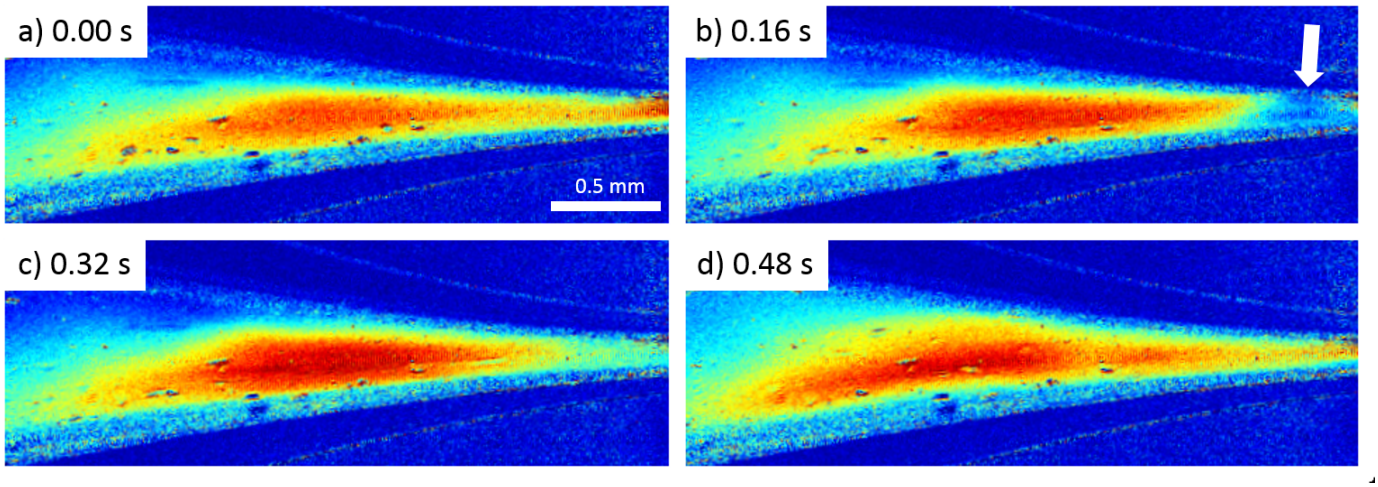

Fig. 6 Retardation magnitude images of CPCL in the capillary entrance (C_1) at t=0, 0.16 s, 0.32 s, 0.48 s. Warm colors indicate larger retardation. The first frame shows a strongly birefringent sample throughout the taper, at t=0.16 s a sharp cleave is observable. The next two frames show the subsequent flow of micelles after the rupture. Note that the spot-like features are stationary. The fluid itself is flowing rapidly. For example, the residence time of the volume exhibiting sudden rupture is approximately 0.05 s.

WLM structure occurs over a short period of time, which has been measured to be of the order (0.01 to 0.1) s[74]. This timescale is comparable to the rapid increase in flow rate, which occurs over approximately 0.1 s (Figure 6), which is observed for each surfactant system. The fast structural change is a necessary condition for the type and magnitude of fluctuations we observe, although if the structural breakdown is faster, it could stabilize a steady state breakage and thus suppress flow fluctuations[73]. The location of breakage further supports disturbance occurs at a streamwise position at $X \approx 3$ cm from the entrance of the tapered region, a location close to the maximum Wi number in entrance shown in Figure 5a. The correspondence between the maximum Wi number suggests that this sharp change in micelle structure occurs at a critical extension rate.

The rupture of WLM solutions in extensional flow has been shown to depend on strain[58]. The maximum strain for capillary contractions can be estimated by $\varepsilon_{max} = \ln(A_{wide}/A_{narrow})$, where A_i is the cross sectional area of the capillary. As can be seen from Table 1, the maximum strain is in the range of $\varepsilon_{max} \approx 2.6 - 4.3$, which is comparable to the range of the total Hencky strain where rupture of a filament has been observed, $\varepsilon_{max} \approx 2.5 to 3$ [58,60,61,75]. The larger critical Wi number observed in capillary C_2 compared with C_1 for CPCL surfactant may be attributable to the difference in contraction ratio, and therefore strain, between these two capillaries. A smaller contraction ratio may require a greater strain rate to produce micelle breakdown or may not provide a sufficient strain to induce rupture. In the future, we plan to investigate the dependence of contraction ratio/maximum strain on the critical Weissenberg number for a wider range of contraction ratios.

3.4 Flow of Polymer Solutions Through an Axi-Symmetric Constriction

In this section we investigate whether the temporal fluctuations observed in the tapered geometry are limited to WLM solutions by testing other viscoelastic solutions, namely a PAA solution and a yield stress gel. The yield stress fluid does not flow until a critical pressure is applied. Once the flow is initiated, no temporal or spatial instabilities were observed in the tapered region. The long-chain polymer PAA solutions are highly elastic, but are only weakly shear thinning due to the high solvent viscosity. Furthermore and importantly, the polymers do not experience chain scission. These long chain polymer solutions are often used to study viscoelastic instabilities in microfluidics[76,77]

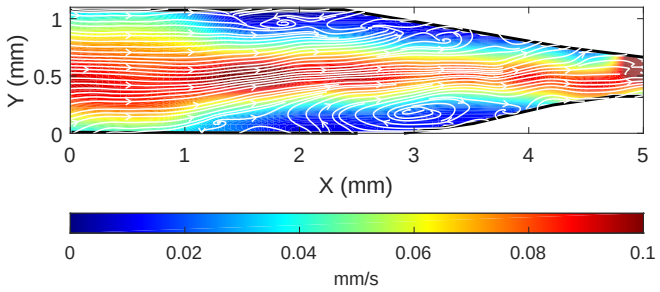

Fig. 7 Spatially unstable flow of PAA into a tapered contraction.

The PAA solutions exhibit spatial instability at the entrance of the tapered region similar to previously observed viscoelastic instabilities observed at entrance regions[78]. A separation zone forms between an inner jet of fluid moving through the center of the tapered region surrounded a long recirculation region which drives fluid away from the entrance region along the channel walls, see Figure 7. As flow rate increases, the recirculation zones extend farther upstream from the entrance region, reaching in excess of 1 cm from the entrance at the highest mean flow rates. Although the instability can occupy a larger portion of the upstream channel, temporal oscillations were not observed in PAA at any flow rate.

In the case of polymer solutions, the spatial instability is a result of a transition of the polymer chains from a coiled state to an extended state[57,79]. The wide range of viscoelastic instability behaviors observed in Couette geometries and pipe flow using polymer solutions suggests that temporal instabilities may be possible in our channels. However, no such fluctuations were observed within the range of applied pressures accessible by our experiment. For the current experiment, the comparison between polymers and WLM solutions demonstrates that the structural breakdown characteristic of WLMs is an essential element for the large magnitude spurt behavior.

3.5 Characterization of Fluctuations

We now analyze the characteristics of the fluctuations above the instability threshold. This includes the spurt magnitude, the time between spurt events, and the relationship between spurt magnitude and pressure. The magnitude of flow fluctuations is $\Delta Q = \max(Q) - \min(Q)$, where the maximum and minimum are taken over a time series. The flow fluctuations are normalized by a characteristic volume representative of the jetting flow in the entrance region, $\pi l r^2$, and the time is scaled by the fluid relaxation time. This magnitude rises abruptly at the instability threshold (see Figure 8), and then rises more slowly at higher flow rate. This trend appears to be true for all systems over the range studied, but the scaling shows that the fluctuation magnitude depends primary on entrance geometry and fluid relaxation time. With these traits in mind, a function of the form $f(x) = A(1-1/x)$ for $x > 1$ with $A = 30$ represents the data well and shows that the fluctuation magnitude is limited by the volume of the entrance region. Only the abrupt contraction shows a deviation from this behavior, which may be a result of an approximate scaling of the upstream radius for the entrance length l or the slightly different jetting behavior discussed in Section 3.7.

The effect of rheological behavior of fluids (see Figure 1) on the relative magnitude of flow fluctuations is mainly controlled through the relaxation time. For example, even though CTAT does not exhibit very strong shear thinning nor a shear stress plateau, its flow fluctuations scale well with relaxation time when compared to CPCL and of CTAB, which both have a stress plateau. Similarly, the relative width of the stress plateau, does not seem to matter much. The relative flow rate fluctuations are similar for the CPCL and CTAB surfactant solutions, even though the stress plateau of the CPCL solution is significantly broader. We note that the CTAB surfactant system exhibits the most regular quasi-periodic behavior of the three surfactant systems that we studied. The other two surfactant systems, CPCL and CTAT, have similar single instability events at mean flow rates just above the transition to unstable flow, but the wait times between events is irregular.

The syringe pump controlled flow of CPCL through the C_1 capillary shows a slightly lower fluctuation magnitude in comparison to the pneumatically controlled flow of the same system. For an incompressible fluid flow through a perfectly rigid system driven by a syringe pump the global flow should be conserved. In the real experiment, any compliance in the flow system including the syringe, tubing, and connectors may allow for changes in volume which will make the local flow rate fluctuate. The syringe pump driven flow appears to reduce the largest magnitude fluctuations, but does not eliminate the fluctuations overall.

The spurt events provide useful markers in the timeseries for quantifying temporal characteristics of the fluctuations. We focus on the CTAB system because it has the most varied behavior of the surfactant systems, particularly the transition from quasi-periodic to chaotic fluctuations. We measure the time between local maxima between events, denoted as Δt, determined from the pressure data. The distribution for Δt at various flow rates above the critical flow rate for fluctuations are shown in Figure 9.

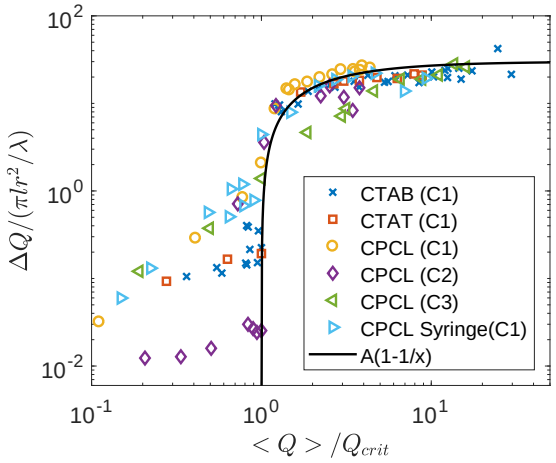

Fig. 8 The magnitude of flow rate fluctuations $\Delta Q = \max(Q) - \min(Q)$, normalized by $\pi l r^2/\lambda$, versus the relative mean flow rate, normalized by the critical flow rate Q_{crit}. The scaling of the flow rate fluctuations is representative of the volume of the jet formed in the entrance region. The data are compared to a function of the form $f(x) = A(1-1/x)$ for $x > 1$ with $A = 30$.

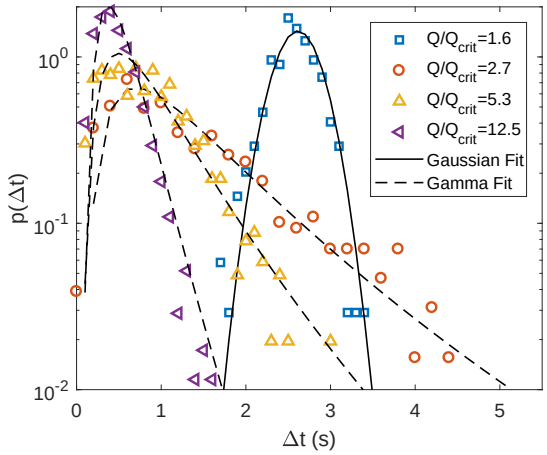

Fig. 9 Probability density distributions of time between events (Δt) determined from pressure data for different flow rates above critical flow rate. Shown with fits for a Gaussian distribution for $Q/Q_{crit} = 1.6$ and Gamma distribution fits for higher flow rates. The gamma distribution values are $\alpha = 2.39$ and $\beta = 0.58$ for $Q/Q_{crit} = 2.7$, $\alpha = 2.94$ and $\beta = 0.30$ for $Q/Q_{crit} = 5.3$ and $\alpha = 4.90$ and $\beta = 0.11$ for $Q/Q_{crit} = 12.5$.

The quasi-periodic data results in a narrower distribution of wait times than the chaotic behavior at higher flow rates. The quasi-periodicity results in a distribution that fits a normal distribution with mean at $\Delta t = 2.6$ s and standard deviation $\sigma = 0.27$ s. The transition to chaotic behavior at higher mean flow rates is clearly shown by the change in the form of the wait time distributions. In particular, the short events become more likely and an exponential tail is observed for longer wait times, a signature of intermittent behavior[80]. A Gamma distribution is chosen to approximate the wait time distributions because of the exponential tail. The Gamma distribution is defined as

$$p(\Delta t|\alpha,\beta) = \frac{1}{\beta^{\alpha}\Gamma(\alpha)}\Delta t^{\alpha-1}\exp(-\Delta t/\beta). \quad (1)$$

The lowest chaotic flow rate has a wider distribution than the higher flow rates, which have shorter time between events and narrower distributions. The fluctuations for the other surfactant systems are not shown, but their wait time distributions are similar with the same trend of decreasing time between spurt events.

We now focus on the conditions which lead to a spurt event. We determine the critical pressure, P_{crit}, by finding the local maximum pressure that coincides with a spurt event. The distribution of critical pressures are plotted in Figure 10(a) and compared to a Normal distribution after being normalized by the fitted standard deviation. Data from both quasi-periodic and chaotic behavior fit the Normal distribution. The critical pressure at which the fluid viscosity decreases dramatically is analogous to the critical stress at which the micelle solutions increase in shear rate. After each spurt event, the flow field and structural arrangement of the micelle varies and can lead to variation in the pressure drop at which the subsequent spurt is triggered. The normal distribution indicates that the conditions in the taper have random variations which lead to the distribution of critical pressures.

The width of the critical pressure distributions are indicative of a range of conditions which can lead to a spurt event. The width of the distributions are plotted in Figure 10(b) for the three surfactant systems in the C_1 channel. At the low mean flow rates, it is apparent that the pressure must build to a critical value for the flow to become unstable. The pressure appears as the limiting parameter for the flow to become unstable. At higher flow rates, the fluid in the taper is highly susceptible to instabilities and can become unstable at all pressure values. To quantify this transition, the standard deviation for the critical pressures is normalized by the standard deviation for the entire pressure time series and plotted as a function of mean flow rate in Figure 10(b) . When normalized in this fashion, the data plateaus at a relative value of $\mathrm{std}(P_{crit})/\mathrm{std}(P) = 1$. Only at low mean flow rates is the range of critical pressures smaller than the overall range of pressures experienced by the system. This is most apparent with the CTAB system, which has a narrow distribution of critical pressures during quasi-periodic flow but broadens when chaotic behavior begins.

The time series and phase diagram shown in Figure 4 demonstrate that flow spurts are related to the buildup and release of pressure brought on by micelle breakage. To investigate this relationship, we compare the spurt magnitude, ΔQ and the critical pressure at which the spurt occurs. In order to compare different mean flow rates, we plot spurt magnitude as a function of the critical pressure shifted by the mean critical pressure, $P_{crit} - < P_{crit} >$, in Figure 11. A linear relationship between the spurt magnitude and the critical pressure is observed for all chaotic systems. When the flow is quasi-periodic, i.e. when $Q/Q_{crit} = 1.5$, the critical pressure and spurt magnitude do not vary much, but these limited variations remain consistent with the same relationship between critical pressure and spurt magnitude. This relationship between pressure and flow rate jumps suggests that larger pressures may cause more extensive breakup of micelles, perhaps to a greater degree and/or in a larger fraction of the entrance volume, reducing the effective viscosity.

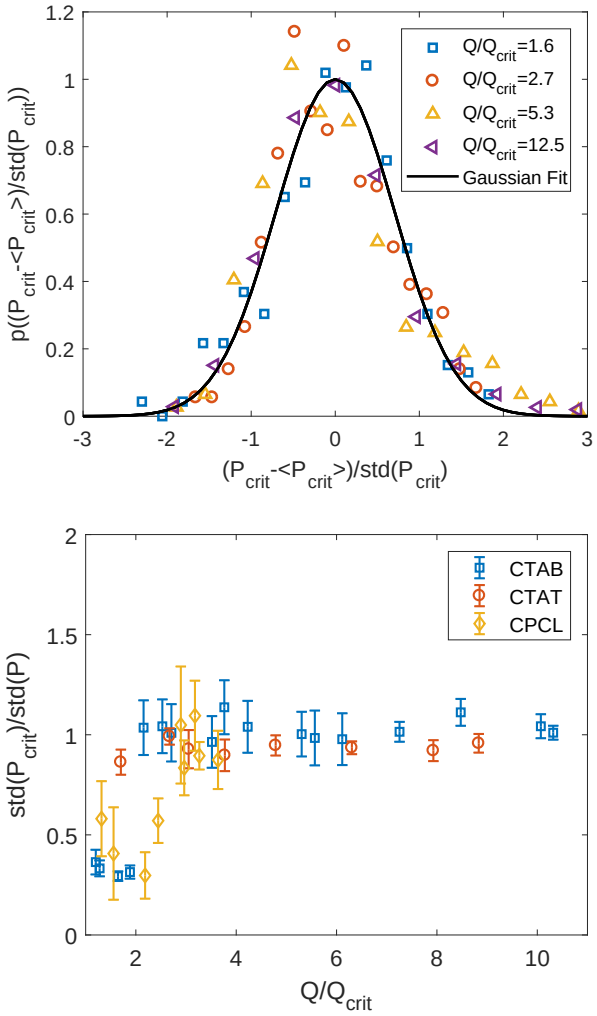

Fig. 10 (a) Distribution of critical pressure values compared to a Normal distribution for the CTAB system in channel C_1. The critical pressures follow a normal distribution for all flow rates. (b) The standard deviation is normalized by the standard deviation of all the pressure data. The uncertainty reflects 95 % confidence intervals on the fit to the standard deviation.

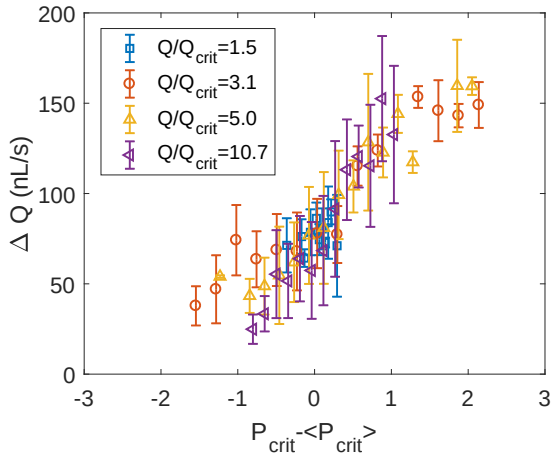

Fig. 11 The mean magnitude of the spurt flow rate jump as a function of the critical pressure shifted by the mean critical pressure for the CTAB system in channel C_1. Error bars represent one standard deviation of the sampled flow rate jumps. A linear relationship is observable at higher mean flow rates showing chaotic behavior. The lowest flow rate, undergoing quasi-periodic behavior, shows relatively lower variation in pressure and corresponding spurts.

3.6 Power Spectra

The fluctuation characteristics of viscoelastic instabilities are often characterized by the power spectral density (PSD)[43,45,81]. The power spectrum for both pressure and flow rate data at various mean flow rates above the critical value are shown in Figure 12. The PSD for each system transitions from a plateau at low frequencies to a power law decay at higher frequencies. The power law exponent for the pressure is approximately -4, while the flow rate shows a less steep exponent of approximately -2 at intermediate frequencies before transitioning to an exponent of -4. When the flow is quasi-periodic, e.g., at $Q/Q_{crit} = 1.4$, the PSD exhibits a characteristic frequency peak, while at higher flow rates this peak is no longer present (Figure 12). As mean flow rate increases, the transition frequency from plateau to power law behavior shifts to higher frequencies, a result of the shorter fluctuation durations seen at higher mean flow.

Power law behavior at high frequencies is often observed in fluctuating systems, in particular chaotic and turbulent fluid flow[82–84]. In contrast to instabilities observed in Couette flow, where many regions of instability can exist simultaneously throughout the gap, the fluctuations observed in the capillary are slightly different in the sense that the pressure and flow rate are a consequence of an isolated (entrance) region undergoing an instability. The time series of pressure and flow rate fluctuations shown in Figure 4 bear similarity with two-sided exponential pulses, which switch between relaxation towards high and low values. Recent work has investigated the power spectrum of similar pulse trains with various waiting time distributions[85]. For the case of a two-sided exponential pulse, the power spectrum is given by :

$$\mathrm{PSD}(f) = \frac{1}{[1+((1-\delta)f\tau)^2][1+((\delta f\tau)^2]}, \qquad (2)$$

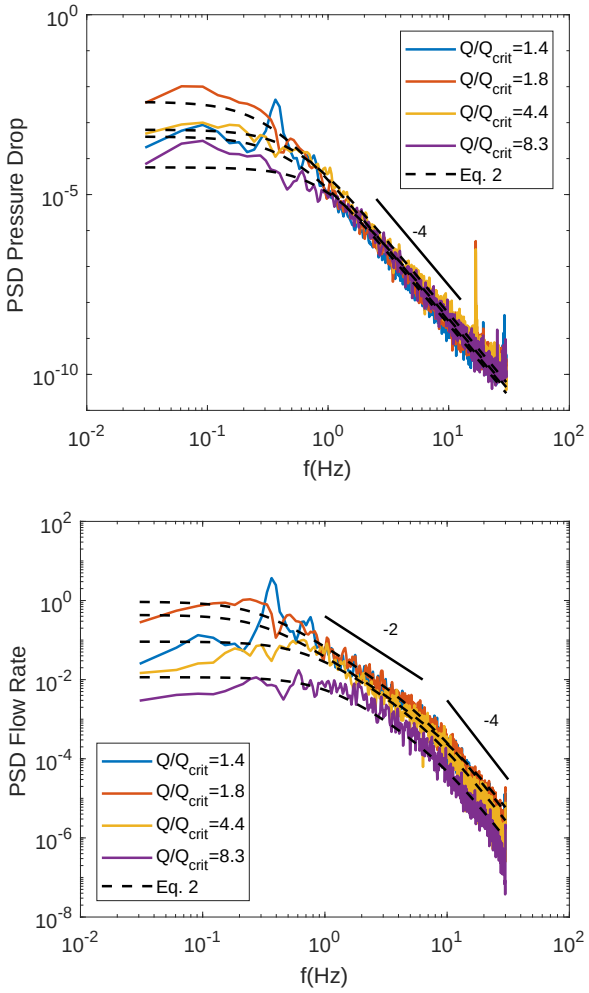

Fig. 12 Power spectrum from (a) pressure and (b) flow rate for the CTAB solution in channel C_1.

where δ is the duty cycle for the pulsed system and τ is the characteristic timescale of the exponential function. This matches the observed response of constant amplitude at low frequencies that transitions to a power law decay at frequency, δ/τ or $(1-\delta)/\tau$, whichever is larger. If δ is close to 0.5, the power law decay at frequencies higher than the transition frequency will have a -4 exponent. If the duty cycle is asymmetric, the characteristic frequency where the transition to a power law shifts and there will be an intermediate power region with -2 exponent.

Fits to Eq. 2, shown in Figure 12, demonstrate fairly good agreement with the experimental PSDs. The duty cycle is determined by measuring the fraction of time with increasing values over each event cycle. The pressure signal is nearly symmetric for most flow rates, except near the critical condition, and a power law at high frequencies with a -4 exponent is expected from Eq. 2. In contrast, the flow rate data is asymmetric, with relatively short times for increasing flow rate compared to the overall cycle. As a result, the power spectrum for the flow rate has an intermediate power law region with -2 exponent. At frequencies that correspond to the fast response of the spurt dynamics, the power law changes to -4. Only the quasi-periodic data show a signifi-

cant deviation from Eq. 2 due to the peak in the power spectrum. We also note that the distribution of waiting times does not significantly change the power spectrum and the power spectrum is more sensitive to the characteristics of the pulse relaxation and the duty cycle[85].

While the power spectra provide a useful characterization of the fluctuation, this analysis assumes that the fluctuations are two-sided exponential pulses. Without more detailed knowledge of the system behavior, the information determined from the timescales using Eq. 2 is limited. In section 4, we introduce a dynamical model that reproduces similar fluctuating behavior and provides a more accurate method for determining characteristic timescales of the fluctuations

3.7 Flow field in an abrupt contraction

The results from section 3.5 showed that the fluctuation magnitude for the abrupt contraction was the smallest of any entrance geometry tested. We investigate the flow field in the C_3 capillary more closely by performing PIV measurements immediately upstream of the entrance to the narrow capillary section.

Unlike the tapered channel, where a high velocity jet forms along the wall of the tapered region, in the abrupt contraction a jet extends from the entrance into the wide section, see Figure 13. At low mean flow rates, the jet is temporally stable and extends about 1.5 mm back from the narrow channel entrance, slightly longer than the one channel diameter. A recirculation region forms in an annular region surrounding the jet. Above the critical flow rate, the position and velocity of the jet begin to fluctuate. Similar to the flow behavior observed in the taper, the jet transiently develops in one direction before dissipating and then developing in another. A weaker jet expelling fluid from the entrance region forms along the opposite side of the inward jet. The off-center orientation of the jet produces a dominant recirculation zone along the adjacent side. This behavior is similar to that observed by Hashimoto et. al.[54].

The flow fields in Figure 13 provide insight into the smaller flow disturbances measured in channel C_3. The jetting instability is localized to a region less than two channel diameters from the entrance and does not extend farther even at higher mean flow rates. In addition, the jet is similar in diameter to the narrow capillary section rather than scaled to the diameter of the entrance region, which appears to be the case in the tapered region. As a result, the volume that is susceptible to temporal instabilities is relatively small compared to tapered entrances.

While the abrupt entrance results in the largest streamline curvature for a given reduction in channel diameter, the smaller entrance region and the characteristics of the jetting flow produce a much smaller flow disruption than the tapered entrances. This is in contrast to the flow of polymer fluids through contractions, which can become unstable in abrupt contractions due to singularities and large streamline curvatures that occur at entrant corners[??]. In the case of our experiments with WLM solutions, the unstable flow is related to a critical extension rate. Increasing the entrance length reduces the extension rate, but also appears to produce large flow fluctuations once triggered. It may be possible

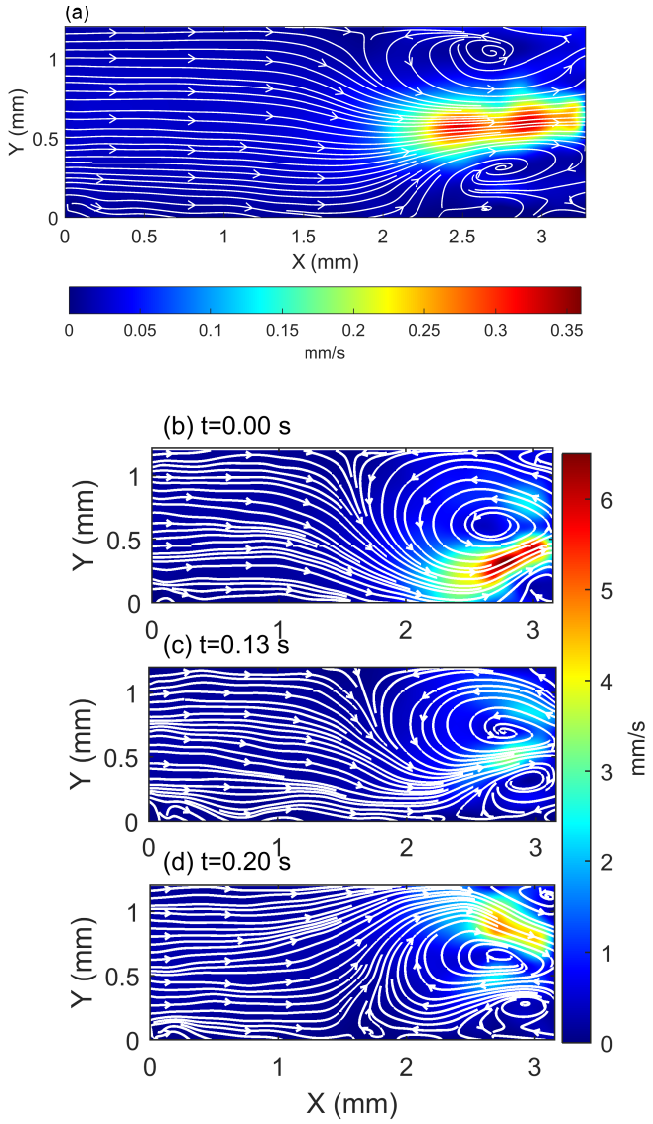

Fig. 13 Jetting flow of CPCL into an abrupt contraction, the entrance to a 150 μm capillary begins at the center right edge of the images. (a) Temporally stable jetting flow. (b) Temporally unstable jetting flow into the narrow capillary. The orientation of the inward flowing jet fluctuates with time.

to reduce channel diameter without instability through a series of small constrictions that remain below a critical strain rate. If smaller temporal instabilities can be tolerated for a flow system, our observations suggest that shorter entrance length contractions, such as an abrupt contraction or a short taper, will reduce the magnitude of temporal fluctuations.

4 Dynamical System Model

The results in Section 3.5 demonstrated that the flow and pressure fluctuations are closely related. We characterize the cycle of fluctuations into three distinct periods, starting from the spurt phase of the cycle, which is triggered at a critical pressure and produces a rapid increase in flow rate. The flow field at that moment in the taper shows that some portion becomes fluidized and rapidly passes through the entrance. During the spurt phase, the

pressure remains nearly constant.

The end of the spurt event is reached when the flow rate reaches a maximum, after which a release phase begins where both the pressure and flow rate decrease. The decrease of flow can be attributed to a finite amount of time required for the fluidized region to completely exit the tapered region. The escape of this fluid corresponds to a decrease in pressure because a volume of lower viscosity fluid flows through the taper and narrow region. The second phase completes when the pressure reaches a minimum and begins to grow again.

During the third phase of the cycle the pressure increases while the flow rate continues to decrease or remain nearly constant at a low flow rate. This pressure build up corresponds to entangled micelles refilling the taper, where the higher viscosity fluid increases the pressure drop across the capillary. The pressure continues to build until a critical value is reached, triggering another spurt event and completing the cycle. We tentatively attribute the observed variation in the critical pressure to a new micelle structure in the taper during each cycle; the structural integrity varies.

We aim to develop better understanding of the relation between pressure and flow rate during this cycle using coupled evolution equations. Similar low-dimensional dynamical models have been used represent nonlinear behavior in both shear- thinning and shear-thickening solutions and for unstable flow in polymer extrusion [86–88] This approach has also been used by Fielding and Olmsted (2004) to describe the spatiotemporal instabilities of a shear banding fluids in a stress controlled Couette flow [42]. Their model couples the evolution of local shear rate and a structural parameter related to the breakage of micelles. Chaotic behavior can also be observed in these models with sufficient degrees of freedom, such as when spatial gradients were included [42,86,89]. Here we describe a low-dimensional dynamical model which represents the characteristics of the system fluctuations, such as the transition from quasi-periodic behavior to chaotic flow and the induction phase observed in Figure 4.

The dynamical models for unstable Couette flow relate the temporal evolution of stress, shear rate, and structure. In our observations (with the exception of optical retardation measurements) we do not directly measure the micelle structure. Nevertheless, the pressure and flow rate measurements are a global measure of the stress and velocity fields and how these two quantities relate provides information about the system behavior. Observation of the trajectory on the P vs Q phase map immediately after the spurt provides the clearest information about this relationship. The minimum in the pressure is an indication that system is crossing a stability curve, represented as nullclines for the pressure, $\frac{\partial P}{\partial t} = 0$. We observe that the pressure minima have a dependence on flow rate that can be represented as a power law, $P_{eq} = AQ^m$. The stability curve for the flow rate evolution equation is chosen to have a linear dependence on pressure, $Q_{eq} = kP$, where k is an inverse of the channel resistance. The linear dependence assumes the flow of micelles in the quasi-Newtonian fluid state.

The fixed point for the system, the values at which the system is stable, occurs where the two nullclines intersect. The evolution equations are given by,

$$\begin{aligned} \frac{\partial P}{\partial t} &= \frac{1}{\lambda_P}\left[AQ^m - P\right], \\ \frac{\partial Q}{\partial t} &= \frac{1}{\lambda_Q}\left[kP - Q\right]. \end{aligned} \tag{3}$$

where λ_P and λ_Q are characteristic timescales for pressure and flow rate respectively.

Without a perturbation, this system of equations will relax towards the fixed point, which in terms of pressure is at the value $P_{fix} = k(Ak)^{1/(1-m)}$. The system is prevented from reaching this equilibrium by producing a jump in flow rate at a critical pressure P_{crit}. If P_{fix} is greater than P_{crit}, the system will oscillate and never reach the fixed point. In order to represent the decrease in the viscosity triggered by the micelle breakage, the fluid resistance term k is changed to a higher value for a fixed duration defining the spurt phase. After the spurt phase is completed, the resistance term is adjusted back to its previous value.

In the experiments we observe a distribution of pressures at which the spurt is triggered (see Figure 10). Each cycle has a different critical pressure which depends on the structure of the fluid in the taper. In order to capture this variability, we sample the critical pressure in the model from the measured distribution, see Figure 10a, and change this value at the moment of the pressure minimum of each cycle. The magnitude of the flow rate jump is linearly related to the critical pressure relative to the mean critical pressure following the relationship given in Figure 11. Both pressure and flow rate quantities are normalized in order to demonstrate the relative magnitude of the fluctuations. The pressure data is normalized by the mean critical pressure, $< P_{crit} >$ and the flow rate is normalized by the maximum stable flow rate, given by $Q_s = k < P_{crit} >$.

We compare the model system to our experimental measurements for different surfactant systems at various mean flow rates. The parameters to fit for the system of equations are the two relaxation timescales, λ_Q and λ_P, and the forcing term parameters, A, m, and k. Simultaneously fitting the pressure and flow rate is performed using nonlinear least square curve fitting in MATLAB. The data are fit during each cycle beginning immediately after the spurt has ended, determined by the local maximum in the flow rate, and concludes at the beginning of the spurt, determined by the large rate of change of the flow rate.

Phase-space plots of pressure drop as a function of flow rate of the experimental and model results exhibit the same behavior with similar fluctuations (Figure 14). The nullclines for pressure and flow rate are shown in dashed and dotted lines, respectively. The system cannot reach the fixed point because the spurt is triggered first.

When the flow is just above the threshold for instability, $Q/Q_{crit} = 1.2$, the fitted nullclines result in a fixed point close to the critical pressure, see Figure 14(a). A spurt is triggered over a narrow range of critical pressures and the system follows a nearly consistent trajectory across the phase space. This situation replicates the quasi-periodic behavior observed with the CTAB surfactants, more easily seen in the time series of the same

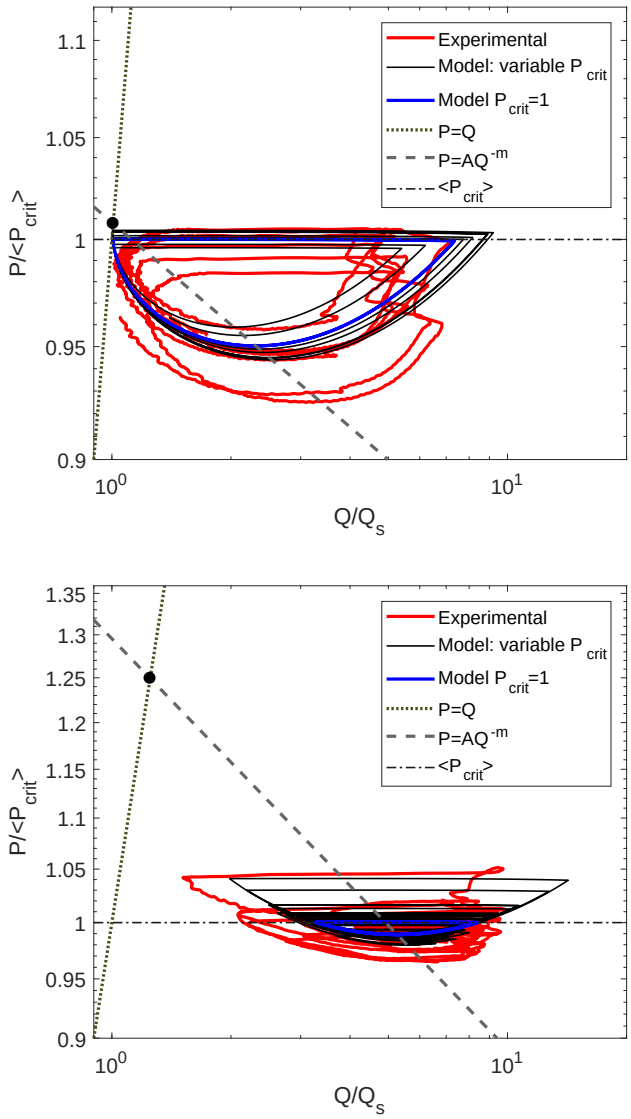

Fig. 14 Phase space plot of the pressure as a function of flow rate for the CTAB system at (a) $Q/Q_{crit} = 1.2$ and (b) $Q/Q_{crit} = 3.8$. The data is fit to Eq 3 to obtain parameter values and then a trajectory is obtained by integration of the model with and without variation in the critical pressure. At low mean flow rates the fixed point is close to the critical pressure and a quasi-periodic behavior is observed (a). The fixed point moves to away from the critical pressure at higher mean flow rates (b). The system fluctuations around the intersection between the mean critical pressure and the nullcline given by $P = AQ^m$.

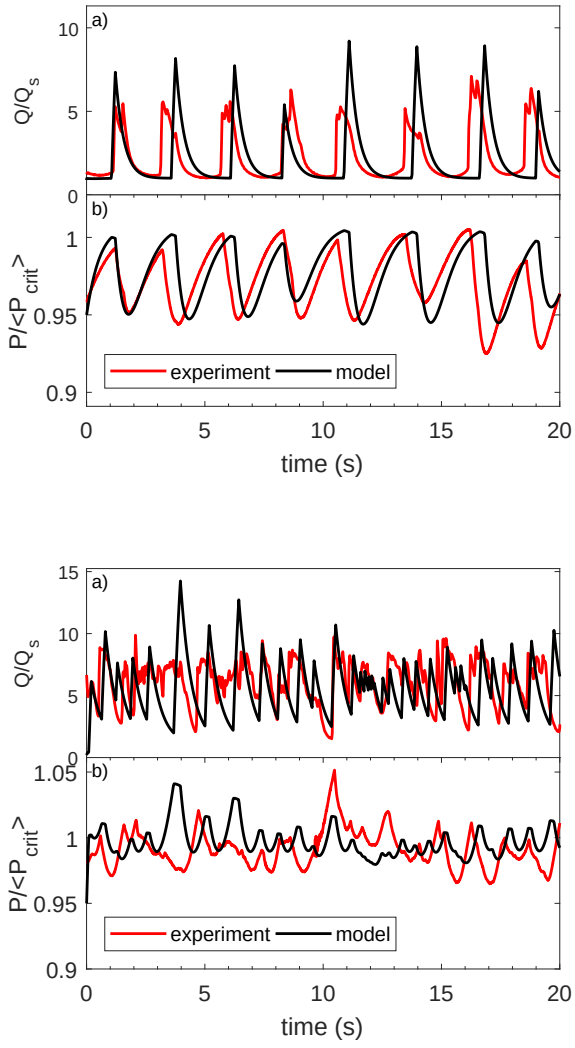

Fig. 15 Time series of the (a) flow rate and (b) pressure shown for the CTAB system in red and model system in black. The experimental data are shown at (left) $Q/Q_{crit} = 1.2$ and (right) $Q/Q_{crit} = 3.8$. The model replicates quasi-periodic behavior at low mean flow rate and chaotic behavior at higher mean flow rate.

data shown in Figure 15(a). The model also replicates the slight increase in the flow rate observed in experiments before the spurt is triggered, see Figure 14(a). This induction period occurs when the system reaches the $P = kQ$ below the critical pressure. As the pressure increases, the system will follow the nullcline and result in a slow increase in flow rate before triggering the spurt instability. This results in the flow rate reaching a local minimum that doesn't coincide with the triggering of the spurt. This induction period becomes longer when the flow rate relaxes faster than the pressure drop following the spurt phase. While the model does not fully capture the duration of this induction period in Figure **??**(a), likely the result of our assumption for the functional form of the stability curves, the model shows that this behavior is a result of the buildup of pressure in the system along the $P = kQ$ nullcline.

When the mean flow rate is increased, the $P = AQ^m$ nullcline shifts relative to the critical pressure. An example of the limit cycle at the higher mean flow rate is shown Figure 14(b). The position of the fixed point shifts away from the critical pressure, and the system orbits around the $P = AQ^m$ line just below the critical pressure. A wider distribution of critical pressures triggers subsequent spurts after only a short relaxation phase but when the pressure remains high. This results in a sequence of spurts at a high flow rate with a small reduction in pressure after each spurt. When the pressure reaches sufficiently below the critical pressure, the system builds in pressure as the flow rate decreases.

The spurt is triggered when the critical pressure is reached again, and the system has time to reach a low flow rate and high pressure state. This shows that the transition from quasi-periodic behavior to chaotic behavior is a result of the transition to a cascade of multiple rupture events that occur when the system is far from the stable fixed point. In addition, the system does not undergo an induction period because the pressure exceeds the critical pressure and becomes unstable before reaching the equilibrium $P = kQ$ line.

An analysis of the flow rate and pressure timescales shows variation as a function of mean flow rate and for different geometries. The λ_P timescale is in the range of (0.2 to 2) s, with the longest timescales fitted from the long taper capillary, C_1. There is a slight decrease of the λ_P timescale with increasing flow rate for all systems. The λ_Q timescale is in the range of (0.1 to 0.7) s for all systems and with the longest timescales from the long taper capillary. There is little variation with flow rate for the λ_Q timescale. We observe a small difference between the CTAB and CPCL systems in the long taper, $\lambda_Q \approx 0.25$ s for CPCL compared to $\lambda_Q \approx 0.5$ s for CTAB. This difference is small considering that the instability occurs at greater flow rate for the CTAB surfactant than the CPCL surfactant and the relaxation time is shorter for the CPCL system. A greater difference is observed in the timescale for the CPCL in the short tapered C_2 capillary, with timescales 3 to 6 times faster than the longer taper C_1.

The dynamical model and fitted timescales are a coarse representation of how the pressure and flow respond to the structural breakdown and recovery that occurs in the tapered region. The sensitivity of the timescale to the entrance shape, and lack of sensitivity to material properties, shows that the geometry where the instability occurs has a dominant effect on the temporal characteristics of the unstable flow. This makes any material property characterization from the flow rate and pressure data difficult in this type of geometry. Nevertheless, the dynamical model provides insight into the relationship between pressure and flow rate not possible from a power spectrum analysis, such as identifying the condition of the fixed point and change in behavior resulting from a shift of the fixed point away from the critical pressure.

5 Conclusions

Our observations show that wormlike micelles through a capillary constriction results in both pressure drop and flow rate fluctuations above a critical mean flow rate. The instability causing these fluctuations occurs due to the significant extensional flow at the entrance region, which results in breakdown of the micelle structure visible using polarized light microscopy. The relationship between extensional flow and micelle breakage is demonstrated through the onset of the instability, which occurs at a similar Weissenberg number for a range of different micelle systems and entrance geometries. The importance of micelle breakage on the spatiotemporal instability is further supported by the lack of fluctuations observed for polymer solutions and yield stress fluids.

In contrast with Couette flow, where the spatiotemporal instability can occur anywhere throughout the gap region, the entrance region in pipe flow localizes the instability to one region of the flow system. The flow rate and pressure fluctuations are a direct effect of the intermittant breakdown of micelles in the entrance region and subsequent refilling and regrowth of the entangled micelle structure. Localizing the instability reduces the effect of multiple concurrent breakdown events, causing the global pressure and flow rate to be suitable indicators of individual instability events in the entrance region.

The freedom for pressure and flow rate to fluctuate locally provide information about how these values are related. In particular, a rapid jump in flow rate begins a pressure release, followed by a recovery phase back to a lower flow rate. The rapid breakdown in micelle structure leads to these dramatic changes in pressure and flow rate. This system trajectory is well illustrated by phase plots of the pressure as a function of flow rate. The phase plots show that the instability is triggered at a critical pressure and prevents the system from reaching a stable fixed point. Using a dynamical systems model to describe the behavior provides a method for measuring the timescales and regions of stability of the lumped system. These timescales are found to depend on geometry of the channel entrance and are not material parameters. Our future experiments will elaborate simultaneous measurements of the fluid structure throughout the cycle using flow birefringence to better inform theoretical models.

Conflicts of interest

"There are no conflicts to declare".

Acknowledgements

We'd like to thank Taka Onuma and Andrew Bridges (Photron) for their assistance in gathering polarized light images.

References

1 S. G. Hatzikiriakos and K. B. Migler, *Polymer processing instabilities: control and understanding*, CRC Press, 2004.
2 W. Hartt, L. Bacca and E. Tozzi, *Wormlike Micelles*, 2017, pp. 379–398.
3 J. S. Weston, D. P. Seeman, D. L. Blair, P. F. Salipante, S. D. Hudson and K. M. Weigandt, *Soft Matter*, 2018, **X**, X.
4 D. V. Boger, *Ann. Rev. Fluid Mech*, 1987, **19**, 57–82.
5 R. G. Larson, E. S. G. Shaqfeh and S. J. Muller, *Journal of Fluid Mechanics*, 1990, **218**, 573.
6 E. S. G. Shaqfeh, *Annual Review of Fluid Mechanics*, 1996, **28**, 129–185.
7 L. Bécu, S. Manneville and A. Colin, *Physical Review Letters*, 2004, **93**, 018301.
8 A. N. Morozov and W. V. Saarloos, *Physics Reports*, 2007, **447**, 112–143.
9 Y. Kim, A. Adams, W. H. Hartt, R. G. Larson and M. J. Solomon, *Journal of Non-Newtonian Fluid Mechanics*, 2016, **232**, 77–87.
10 C. J. S. Petrie and M. M. Denn, *AIChE Journal*, 1976, **22**, 209–236.
11 M. M. Denn, *Annual Review of Fluid Mechanics*, 2001, **33**, 265–287.
12 A. V. Rama Murthy, *Transactions of the Society of Rheology*, 1974, **18**, 431–452.

13 A. F. Méndez-Sánchez, M. R. López-González, V. H. Rolón-Garrido, J. Pérez-González and L. de Vargas, *Rheologica Acta*, 2003, **42**, 56–63.

14 M. Meller, A. Luciani, A. Sarioglu and J.-A. E. Månson, *Polymer Engineering & Science*, 2002, **42**, 611–633.

15 J.-B. Salmon, A. Colin, S. Manneville and F. Molino, *Physical Review Letters*, 2003, **90**, 228303.

16 A. P. R. Eberle and L. Porcar, 2012.

17 J. A. Pathak, D. Ross and K. B. Migler, *Physics of Fluids*, 2004, **16**, 4028–4034.

18 Y. C. Lam, H. Y. Gan, N. T. Nguyen and H. Lie, *Biomicrofluidics*, 2009, **3**, 014106.

19 F. a. Morrison, *Oxford University Press*, 2001, 387–394.

20 C. J. Pipe and G. H. McKinley, *Mechanics Research Communications*, 2009, **36**, 110–120.

21 L. Pan and P. E. Arratia, *Microfluidics and Nanofluidics*, 2013, **14**, 885–894.

22 S. D. Hudson, P. Sarangapani, J. A. Pathak and K. B. Migler, *Journal of Pharmaceutical Sciences*, 2015, **104**, 678–685.

23 P. Pakdel and G. H. McKinley, *Physical Review Letters*, 1996, **77**, 2459–2462.

24 G. H. Mckinley, P. Pakdel, A. Oztekin and G. H. Mckinley, *Non-Newtonian Fluid Mech. J. Non-Newtonian Fluid Mech*, 1996, **67**, 19–47.

25 M. E. Cates and S. J. Candau, *Journal of Physics: Condensed Matter*, 1990, **2**, 6869–6892.

26 M. E. Cates and S. M. Fielding, *Advances in Physics*, 2006, **55**, 799–879.

27 C. A. Dreiss, *Soft Matter*, 2007, **3**, 956.

28 J.-F. Berret, *Langmuir*, 1997, **13**, 2227–2234.

29 R. Makhloufi, J. P. Decruppe, A. Aït-Ali and R. Cressely, *Europhysics Letters (EPL)*, 1995, **32**, 253–258.

30 R. W. Mair and P. T. Callaghan, *Europhysics Letters (EPL)*, 1996, **36**, 719–724.

31 P. D. Olmsted, *Rheologica Acta*, 2008, **47**, 283–300.

32 P. Callaghan, M. Cates, C. Rofe and J. B. A. F. Smeulders, *Nuclear Magnetic Resonance Microscopy. Journal de Physique II, EDP Sciences <10*, 1996, **6**, 375–393.

33 M. M. Britton, R. W. Mair, R. K. Lambert and P. T. Callaghan, *Journal of Rheology*, 1999, **43**, year.

34 V. Lutz-Bueno, J. Kohlbrecher and P. Fischer, 2015.

35 C. G. Lopez, T. Watanabe, A. Martel, L. Porcar and J. T. Cabral, *Scientific Reports*, 2015, **5**, 7727.

36 E. Boek, J. Padding, V. Anderson, W. J. Briels and J. Crawshaw, *Journal of non-newtonian fluid mechanics*, 2007, **146**, 11–21.

37 S. Lerouge and J. Berret, *Polymer Characterization*, 2009.

38 M.-A. Fardin and S. Lerouge, *Eur. Phys. J. E*, 2012, **35**, year.

39 R. Ganapathy and A. K. Sood, *Journal of Non-Newtonian Fluid Mechanics*, 2008.

40 R. Ganapathy and A. Sood, *Physical review letters*, 2006, **96**, 108301.

41 M.-A. Fardin, L. Casanellas, B. Saint-Michel, S. Manneville and S. Lerouge, *Journal of Rheology*, 2016, **60**, 917–926.

42 S. M. Fielding and P. D. Olmsted, *Physical Review Letters*, 2004, **92**, 084502.

43 M. A. Fardin, D. Lopez, J. Croso, G. Grégoire, O. Cardoso, G. H. McKinley and S. Lerouge, *Physical Review Letters*, 2010, **104**, 178303.

44 J. Beaumont, N. Louvet, T. Divoux, M.-A. Fardin, H. Bodiguel, S. Lerouge, S. Manneville and A. Colin, *Soft Matter*, 2013, **9**, 735–749.

45 A. Groisman and V. Steinberg, *Nature*, 2001, **410**, 905–908.

46 Y. Jun and V. Steinberg, *Physical Review E*, 2011, **84**, 056325.

47 S. J. Haward, F. J. Galindo-Rosales, P. Ballesta and M. A. Alves, *Citation: Appl. Phys. Lett*, 2014, **104**, year.

48 P. F. Salipante, C. A. E. Little and S. D. Hudson, *Physical Review Fluids*, 2017, **2**, 033302.

49 J. Zilz, R. J. Poole, M. A. Alves, D. Bartolo, B. Levaché and A. Lindner, *J. Fluid Mech*, 2017, **712**, 203–218.

50 T. J. Ober, S. J. Haward, C. J. Pipe, J. Soulages and G. H. McKinley, *Rheologica Acta*, 2013, **52**, 529–546.

51 S. M. Fielding and H. J. Wilson, *J. Non-Newtonian Fluid Mech*, 2010, **165**, 196–202.

52 P. Nghe, S. M. Fielding, P. Tabeling and A. Ajdari, *Physical Review Letters*, 2010, **104**, 248303.

53 C. Masselon, J.-B. Salmon and A. Colin, *Physical review letters*, 2008, **100**, 038301.

54 T. Hashimoto, K. Kido, S. Kaki, T. Yamamoto and N. Mori, *Rheologica acta*, 2006, **45**, 841–852.

55 V. Lutz-Bueno, J. Kohlbrecher and P. Fischer, *Journal of Non-Newtonian Fluid Mechanics*, 2015, **215**, 8–18.

56 J. López-Aguilar, M. Webster, H. Tamaddon-Jahromi and O. Manero, *Journal of Non-Newtonian Fluid Mechanics*, 2014, **204**, 7–21.

57 J. P. Rothstein and G. H. McKinley, *Journal of non-newtonian fluid mechanics*, 2001, **98**, 33–63.

58 J. P. Rothstein, *Journal of Rheology*, 2003, **47**, 1227–1247.

59 S. Chen and J. P. Rothstein, *Journal of Non-Newtonian Fluid Mechanics*, 2004, **116**, 205–234.

60 G. R. Moss and J. P. Rothstein, *Journal of Non-Newtonian Fluid Mechanics*, 2010, **165**, 1505–1515.

61 H. Mohammadigoushki and S. J. Muller, *Journal of Rheology*, 2016, **60**, 587–601.

62 H. Mohammadigoushki and S. J. Muller, *Journal of Non-Newtonian Fluid Mechanics*, 2018, **257**, 44–49.

63 J.-F. Berret, G. Porte and J.-P. Decruppe, *Physical Review E*, 1997, **55**, 1668–1676.

64 R. A. Sampson, *Philosophical Transactions of the Royal Society of London. A*, 1891, **182**, 449–518.

65 W. Thielicke and E. Stamhuis, *Journal of Open Research Software*, 2014, **2**, year.

66 R. G. Larson, E. S. Shaqfeh and S. J. Muller, *Journal of Fluid Mechanics*, 1990, **218**, 573–600.

67 E. S. Shaqfeh, *Annual Review of Fluid Mechanics*, 1996, **28**, 129–185.

68 P. Pakdel and G. H. McKinley, *Physical Review Letters*, 1996,

77, 2459.
69 G. H. McKinley, P. Pakdel and A. Öztekin, *Journal of Non-Newtonian Fluid Mechanics*, 1996, **1**, 19–47.
70 R. K. Prud'homme and G. G. Warr, *Langmuir*, 1994, **10**, 3419–3426.
71 C.-M. Chen and G. G. Warr, *Langmuir*, 1997, **13**, 1374–1376.
72 P. A. Vasquez, G. H. McKinley and L. P. Cook, *Journal of non-newtonian fluid mechanics*, 2007, **144**, 122–139.
73 A. Kalb, L. A. Villasmil-Urdaneta and M. Cromer, *Journal of Non-Newtonian Fluid Mechanics*, 2018.
74 I. A. Kadoma, C. Ylitalo and J. W. van Egmond, *Rheologica Acta*, 1997, **36**, 1–12.
75 A. Bhardwaj, E. Miller and J. P. Rothstein, *Journal of Rheology*, 2007, **51**, 693–719.
76 L. Pan, A. Morozov, C. Wagner and P. Arratia, *Physical review letters*, 2013, **110**, 174502.
77 B. Qin and P. E. Arratia, *Physical Review Fluids*, 2017, **2**, 083302.
78 A. Lubansky, D. Boger, C. Servais, A. Burbidge and J. J. Cooper-White, *Journal of non-newtonian fluid mechanics*, 2007, **144**, 87–97.
79 J. Pearson, *Annual Review of Fluid Mechanics*, 1976, **8**, 163–181.
80 Y. Jun and V. Steinberg, *Physical Review Letters*, 2009, **102**, 124503.
81 S. Majumdar and A. K. Sood, *Physical Review E*, 2011, **84**, 015302.
82 A. Groisman and V. Steinberg, *Nature*, 2000, **405**, 53.
83 M.-A. Fardin, D. Lopez, J. Croso, G. Grégoire, O. Cardoso, G. McKinley and S. Lerouge, *Physical review letters*, 2010, **104**, 178303.
84 J. Beaumont, N. Louvet, T. Divoux, M.-A. Fardin, H. Bodiguel, S. Lerouge, S. Manneville and A. Colin, *Soft Matter*, 2013, **9**, 735–749.
85 O. E. Garcia and A. Theodorsen, *Physics of Plasmas*, 2017, **24**, 020704.
86 J.-B. Salmon, A. Colin and D. Roux, *Physical Review E*, 2002, **66**, 031505.
87 M. Cates, D. Head and A. Ajdari, *Physical review E*, 2002, **66**, 025202.
88 J. L. Dubbeldam and J. Molenaar, *Journal of non-newtonian fluid mechanics*, 2003, **112**, 217–235.
89 A. Aradian and M. Cates, *Physical Review E*, 2006, **73**, 041508.

Simultaneous flow and pressure fluctuations show the relationship between breakage of wormlike micelles and flow rate jumps in capillary constrictions.